

VIP Very Important Paper

Special Collection

www.batteries-supercaps.org

Enhanced Zn²⁺ Transport in Ionic Liquid Electrolyte by Hydrofluoroether Dilution for High-Power and Long-Life Zn/Graphite Cells

Na Li,^[a] Jia Wang,^[b] Qingwei Zhang,^[a] Xinhong Zhou,*^[a] Hao Wang,^[b] Guoli Lu,^[b, d] Jingwen Zhao,^[b, c] Zheng Chen,*^[b, c] and Guanglei Cui*^[b, d]

Ionic liquid (IL) electrolytes have been widely used in high-voltage Li-based dual ion batteries (DIBs) due to their strong resistance against oxidation. However, their applications in Zn-based DIBs are restricted because the high charge density of divalent Zn²⁺ aggravates the ionic interactions in ionic networks and leads to insufficient Zn²⁺ mobility. Herein, we introduce a hydrofluoroether diluent into a Zn-based IL electrolyte to break down the larger ionic aggregates into smaller ones with weakened ionic interactions. This unique solvation

structure reduces the Stokes radius of Zn²⁺ from 1.3 nm to 0.97 nm and increases its diffusion coefficient by ~30 times while retaining the high oxidation stability, enabling the charge/discharge cycling of Zn/graphite DIBs at a high rate of 20 C. Moreover, the enhanced mobility of Zn²⁺ also promotes compact Zn deposition, which allows the operation of anode-free Zn/graphite DIBs with 90% capacity retention after 100 cycles.

Introduction

Widespread installation of renewable energy sources such as wind, solar and tide has been hampered by the lack of suitable grid scale energy storage solutions.^[1] Dual ion batteries (DIBs), which store energy via anion intercalation into graphite cathodes and simultaneous cation insertion or deposition on the anode, can be very competitive in terms of cost, material abundance, and sustainability for large-scale stationary storage.^[2] Moreover, the pseudocapacitive nature of anion intercalation into graphite endows the DIBs with the additional benefit of high-power capability.^[3] Among various kinds of DIBs,^[4] Zn/graphite DIBs involving Zn/Zn²⁺ anode reactions are particularly promising considering the ideal properties of Zn (electro)chemistry: high volumetric energy density (5851 Ah L⁻¹), easy processing in metallic state and intrinsic

safety.^[5] However, a major challenge is their relatively inferior cycle life due to the inherent high potential of anion intercalation into graphite cathodes (2.1–3.1 V vs. Zn/Zn²⁺).^[6] Up to now, very few organic electrolytes have been reported to “survive” such high potentials without being oxidized and decomposed.^[7] Ionic liquids (ILs), being salts of low temperature melting points, are one of the most promising classes of electrolytes providing new opportunities in high-voltage electrochemistry due to their excellent oxidative stability.^[8] In addition, other merits such as negligible vapor pressure, low flammability and a broad liquid range make them more appealing in DIBs.^[9] In fact, most early research work of DIBs adopted ILs as supporting electrolytes.^[10]

Although a series of Zn-based IL electrolytes have already been developed for Zn plating,^[11] their applications in Zn/graphite DIBs are restricted due to limited Zn²⁺ mobility. Since ILs are entirely composed of ions without the presence of solvent molecules to screen the cation-anion interactions, extensive ionic interactions exist as evidenced by their high viscosity and low ionic mobility.^[12] Compared with monovalent Li⁺, the divalent nature of Zn²⁺ further aggravates the ionic interactions due to its higher charge density.^[13] Accordingly, Zn-based ILs are highly prone to generate large ionic aggregates, which accounts for the limited transport ability of ionic species. Consequently, typical charge/discharge curves of Zn/graphite DIBs using IL electrolytes are featured with large polarizations and relatively low capacities even at moderately high rates.^[14] Furthermore, the insufficient Zn²⁺ transport ability in ILs is unfavorable for compact Zn deposition on the anode side. A general consensus of Zn electrodeposition is that the slow rate of Zn²⁺ transport results in the formation of an ion-depleted extended space charge layer on Zn surface, which leads to a high propensity of rough and non-compact Zn deposition.^[15] Different from compact deposition in which the

[a] N. Li, Q. Zhang, Prof. X. Zhou
College of Chemistry and Molecular Engineering
Qingdao University of Science and Technology
Qingdao 266042 (P. R. China)
E-mail: zhouxinhong@qust.edu.cn

[b] J. Wang, H. Wang, G. Lu, Dr. J. Zhao, Dr. Z. Chen, Prof. G. Cui
Qingdao Institute of Bioenergy and Bioprocess Technology
Chinese Academy of Sciences
Qingdao 266101 (P. R. China)
E-mail: chenzheng@qibebt.ac.cn
cuigl@qibebt.ac.cn

[c] Dr. J. Zhao, Dr. Z. Chen
Shandong Energy Institute
Qingdao, 266101 (P. R. China)

[d] G. Lu, Prof. G. Cui
School of Future Technology
University of Chinese Academy of Sciences
Beijing 100049 (P. R. China)

 Supporting information for this article is available on the WWW under
<https://doi.org/10.1002/batt.202300058>

 An invited contribution to a Special Collection on Fast Charging Batteries

electrolyte has no access to the bottom of deposits, loose and noncompact deposition permits the diffusion of electrolytes to the roots of Zn deposits, which facilitates Zn dissolution from the bottom during the stripping process.^[16] This process irreversibly depletes the Zn metal and results in poor cycling performance of Zn anode at high depth of discharge (DOD_{Zn}). As such, rechargeable Zn batteries employing Zn–ILs is usually cycled at a low DOD_{Zn} to avoid battery failure, which leads to severe underutilization of the Zn theoretical capacity.^[17]

So far, most attempts at improving the transport ability of Zn²⁺ in IL electrolytes have been realized via introducing high-permittivity solvents such as H₂O and DMSO to facilitate the salt dissociation and ion migration.^[11a,18] Nonetheless, these high-permittivity solvents are prone to oxidative decomposition at high potentials, rendering them impractical as cosolvents in IL electrolytes for high-voltage Zn/graphite DIBs. Recently, the concept of “diluted ionic liquid electrolyte” has been developed in Li metal batteries by using hydrofluoroethers (HFEs) as diluents into IL electrolytes to lower the viscosity of and increase the Li⁺ conductivity.^[19] The “inert” HFEs scarcely participate in the solvation of Li⁺ and thus maintain the low polysulfide solubility,^[20] which is crucial for Li–S batteries. Another merit of HFEs as diluents lies in their excellent stability against high-voltage metal oxide cathodes due to the highly fluorinated nature.^[21] Although these studies mainly focus on Li metal batteries, they remind us to explore the possibility of adopting HFEs as diluents to increase the Zn²⁺ transport ability in Zn-based ILs while not compromise their high oxidation stability, which is expected to enhance the rate capability and cycle life of Zn/graphite DIBs.

In this work, we introduce a HFE, namely 1,1,2,2-tetrafluoroethyl 2,2,3,3-tetrafluoropropyl ether, as a diluent to enhance the Zn²⁺ transport ability in a typical Zn-based IL electrolyte composed of zinc bis(trifluoromethanesulfonyl)imide (Zn(TFSI)₂) dissolved in PyrTFSI (Pyr represents N-butyl-N-methylpyrrolidinium). The chemical structures of the anion and cation from ionic liquid as well as the HFE diluent used in this work are shown in Scheme 1. Detailed investigations of the solvation structure reveal that although the “inert” HFE does not participate in the solvation of Zn²⁺, it interacts with Pyr⁺ to weaken the extensive ionic interactions in large ionic networks and thus breaks down the ionic aggregates into smaller ones with reduced Stokes radius of Zn²⁺. As a result, the viscosity is reduced significantly to a more practical level and the diffusion coefficient of Zn²⁺ is increased by ~30 times. The enhanced mobility of Zn²⁺ lowers the overpotential of Zn/Zn²⁺ by ~0.2 V at a current density of 0.1 mA cm⁻², which renders the operation of Zn/graphite DIBs at a high rate of 20 C. More

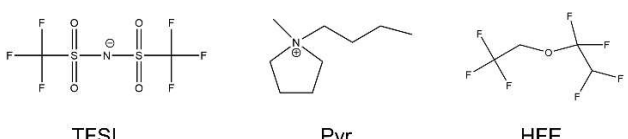
importantly, it also alleviates the concentration polarization and promotes compact Zn deposition, thus enabling the cycling of anode-free Zn/graphite DIBs with 90% capacity retention after 100 cycles.

Results and Discussion

Physical properties of electrolytes

The Zn-based IL electrolyte (abbreviated as Zn–IL) is prepared by dissolving 0.4 M Zn(TFSI)₂ in ionic liquid PyrTFSI. This electrolyte has previously been shown to be incapable of delivering satisfied rate performance of Zn/graphite DIBs due to its low ionic conductivity.^[14] To overcome this challenge, the Zn–IL was mixed with HFE at a volume ratio of 1:1 and the obtained electrolyte was denoted as Zn–IL–HFE. The appearance of a homogeneous solution of Zn–IL–HFE shows that the Zn–IL and HFE are miscible, forming a single-phase liquid (Figure S1). Strong resistance against oxidation is a prerequisite for electrolytes to be compatible with high-voltage Zn/graphite DIBs. Hence, we first evaluated the anodic stability of Zn–IL–HFE on a Ti foil by linear sweep voltammogram (LSV) in a three-electrode electrochemical cell (Figure S2). The anodic decomposition in Zn–IL–HFE electrolyte occurs at an onset potential of 3.50 V vs. Zn/Zn²⁺, which is comparable with that of Zn–IL electrolyte (Figure 1a), signifying the high anodic stability of HFE. As a comparison, conventional organic electrolytes for Zn/graphite DIBs composed of Zn(TFSI)₂ dissolved in ethyl methyl carbonate (EMC) or acetonitrile (AN) solvent suffer from oxidative decomposition at onset potentials of 2.42–2.55 V vs. Zn/Zn²⁺. The high oxidation stability of the Zn–IL–HFE electrolyte enables the superior cycling performance of Zn/graphite DIBs, as 87% capacity retention is achieved after 1000 cycles at a cut-off voltage of 2.65 V with an average CE of 99.2% (Figure S3). As a comparison, the discharge capacity of the Zn/graphite DIB based on Zn–IL electrolyte halved in only 820 cycles, which is likely related to the poor reversibility of Zn plating/stripping as discussed in the later section. In addition, both the ¹⁹F and ¹H NMR spectra of the cycled Zn–IL–HFE electrolyte as well as the online electrochemical mass spectroscopy (OEMS) of the Zn/graphite DIB cell show that the Zn–IL–HFE electrolyte does not suffer from significant decomposition (Figures S4 and S5), further pointing to the high electrochemical stability of HFE.

As a diluent, the extremely low viscosity of HFE is expected to reduce the overall viscosity of Zn–IL electrolyte and thus increase the ionic conductivity. Indeed, even at a volume fraction of 25%, the introduced HFE results in a rapid fall of the viscosity of Zn–IL by an order of magnitude (Figure 1b). When the volume fraction of HFE reaches 50%, the viscosity is further lowered to 28 cP, which is comparable to typical Zn-based organic electrolytes. Ionic conductivity, which quantifies the ion conduction ability, is usually strongly affected by viscosity in terms of ionic migration.^[22] Figure 1(c) shows the ionic conductivity of the Zn–IL electrolyte upon the addition of varied amounts of HFE. Increasing the volume fraction of HFE from 0



Scheme 1. Chemical structures of Pyr cation, TFSI anion, and HFE used in this work.

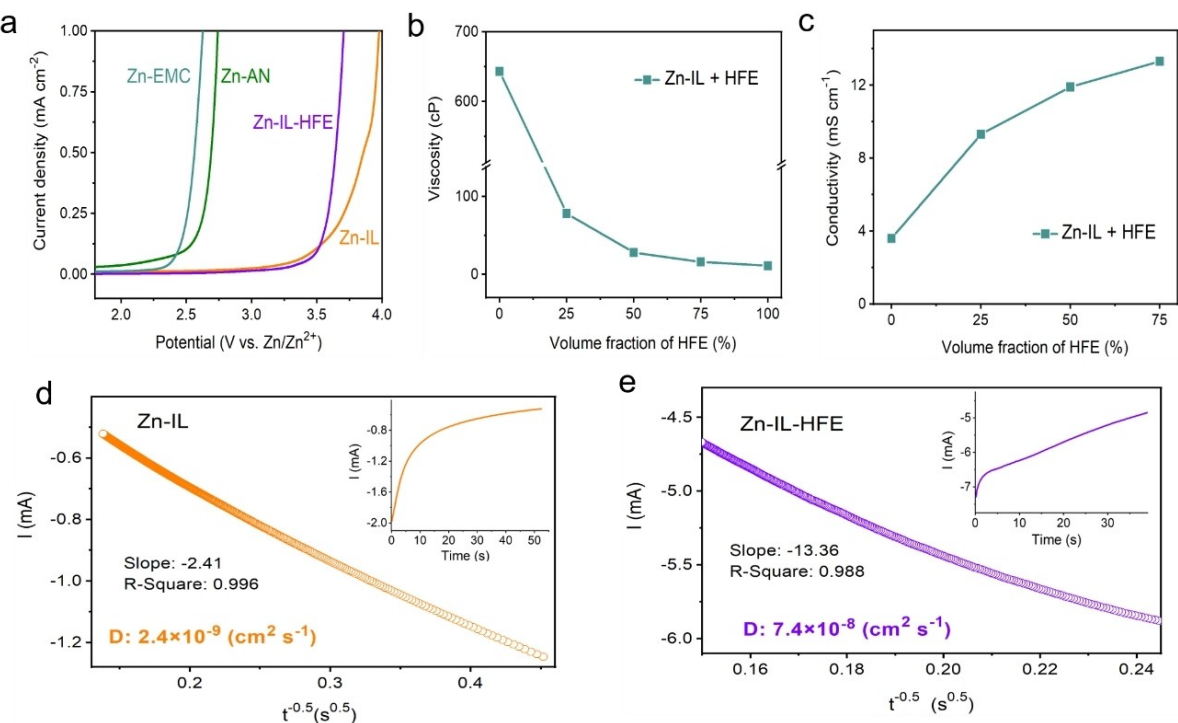


Figure 1. Physical properties of electrolytes. a) LSV curves to compare the anodic stability of varied Zn-based electrolytes. LSV curves were collected at a scan rate of 0.5 mV s^{-1} in a three-electrode cell using Zn foils as the counter and reference electrodes. b) Viscosity of diluted Zn–IL electrolytes at varied volume fractions of HFE. c) Ionic conductivities of diluted Zn–IL electrolytes at varied volume fractions of HFE. Plot of Zn plating current versus $t^{-1/2}$ to calculate the diffusion coefficient of Zn^{2+} in (d) Zn–IL and (e) Zn–IL–HFE electrolytes.^[23]

to 75% results in a rise of ionic conductivity from 3.6 mS cm^{-1} to 11.9 mS cm^{-1} . To quantitatively determine the ionic mobility, chronoamperometry (CA) experiments were performed to measure the diffusion coefficient of active Zn species in a diffusion-limited process via the following Cottrell equation:^[23]

$$i = \frac{nFACD^{\frac{1}{2}}}{\pi^{\frac{1}{2}}t^{\frac{1}{2}}}$$

where i is the current, n is the number of electrons transferred in the reduction process, F is Faraday's constant, A is the planar surface area of the electrode, C is the concentration of the reactive species, D is the diffusion coefficient, and t is the time. The diffusion coefficient can be deduced from the slope of a plot of i versus $t^{-1/2}$. The diffusion coefficient of the active Zn species in Zn–IL electrolyte was calculated to be $2.4 \times 10^{-9} \text{ cm}^2 \text{ s}^{-1}$ based on fitting results (Figure 1d). This value is orders of magnitude lower than typical Li-based ILs, which can be explained by the much enhanced ionic interactions in Zn–IL due to the divalent nature of Zn^{2+} . In comparison, the diffusion coefficient of the active Zn species in Zn–IL–HFE electrolyte reaches $7.4 \times 10^{-8} \text{ cm}^2 \text{ s}^{-1}$ (Figure 1e), which represents an almost 30-fold increment.

Solvation structures of electrolytes

To rationalize the significantly increased diffusion coefficient of Zn^{2+} in Zn–IL–HFE electrolyte, the interactions between HFE and ionic components including Zn^{2+} , Pyr⁺ and TFSI⁻ are worthy of in-depth investigations. It is well known that HFEs are commonly used as "inert" diluents because of their low donor ability (Gutman's donor number < 10) and relatively low permittivity.^[20b] In fact, during the preparation of the Zn–IL–HFE electrolyte, it is noted that HFE can hardly dissolve $\text{Zn}(\text{TFSI})_2$ salt, as evidenced by clear phase separation of white salt powders in the bottom and solvent on top in their mixtures placed in a vial (Figure S6). Since the dissolution of a metal salt is largely dependent on the solvation energy of the cation in aprotic solvents, the extremely low solubility of $\text{Zn}(\text{TFSI})_2$ in HFE suggests that HFE does not solvate Zn^{2+} , in line with the weak solvating power of hydrofluoroethers.^[20b] On the other hand, given that HFE is miscible with Zn–IL, we can deduce that HFE is well dispersed in the ionic structure of the Zn–IL due to interactions between HFE and some ionic species from Zn–IL.

To understand the effects of HFE addition on the local structure of Zn–IL electrolyte on the microscopic scale, Raman spectroscopy was performed. Figure 2(a) shows the Raman spectra of ionic liquid PyrTFSI in the region 700 – 780 cm^{-1} where the band ascribed to the S–N–S stretching vibration from TFSI⁻ is found at 739 cm^{-1} . With the addition of 0.4 M $\text{Zn}(\text{TFSI})_2$ salt, a shoulder peak attributed to TFSI⁻ coordinated to Zn^{2+} appeared at 746 cm^{-1} . Upon the introduction of HFE, no

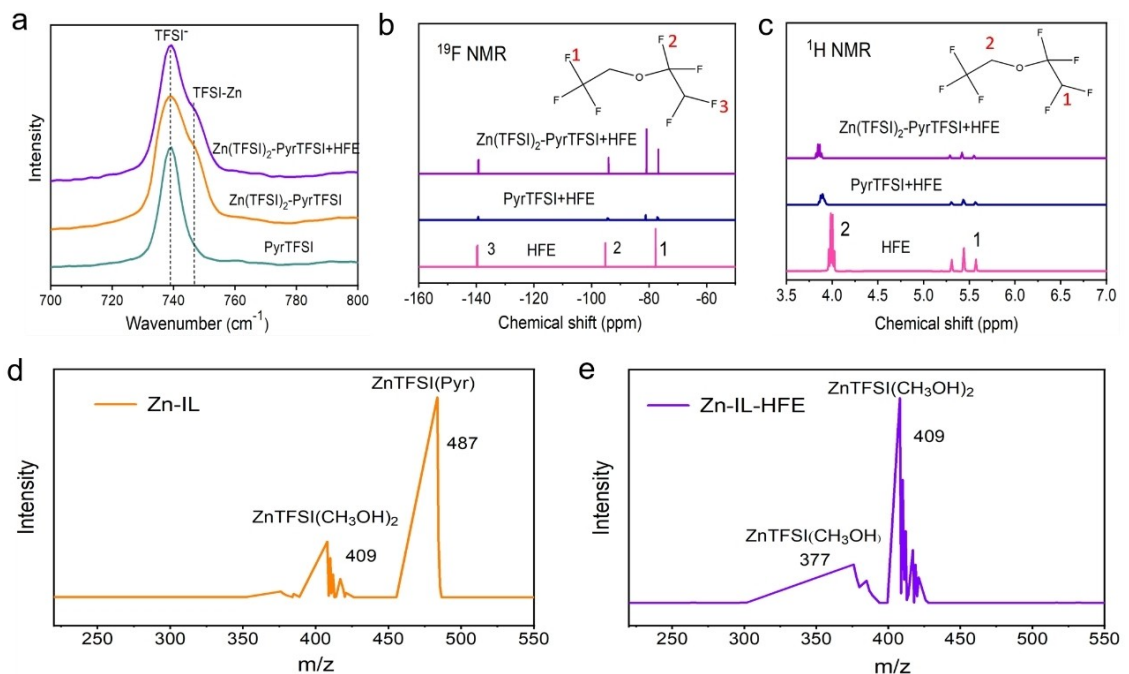


Figure 2. Spectroscopic characterizations of Zn–IL–HFE electrolyte to probe its solvation structure. a) Raman spectra of various components of Zn–IL–HFE electrolyte. b) ^{19}F NMR and c) ^1H NMR spectra to investigation of the interactions between HFE and ionic species in Zn–IL–HFE electrolyte. Electrospray ionization mass spectroscopy (ESI–MS) characterizations of d) Zn–IL and e) Zn–IL–HFE electrolytes in positive ion mode. The electrolyte solution was diluted with methanol in order to obtain the mobile phase before injection into the chamber for ESI–MS tests.

noticeable change of this shoulder peak in terms of wavenumber and relative intensity is observed, indicating that HFE does not interact with TFSI^- . Hence, it is speculated that the well dispersion of HFE in Zn–IL originates from the preferential interaction of HFE with Pyr^+ .

The interactions between HFE and ionic components in the Zn–IL–HFE electrolyte were also investigated by ^1H NMR and ^{19}F NMR. No obvious shift of ^{19}F NMR signals from HFE can be observed upon the addition of ionic liquid PyrTFSI or Zn–IL solution (Figure 2b), indicative the “inert” nature of HFE. Although the ^1H NMR signal of [H1] atom (far away from oxygen atom) from HFE barely changes after the addition of ionic liquid PyrTFSI, the ^1H NMR signal of [H2] atom from HFE show obvious upfield shift by 0.1 ppm (Figure 2c), which reveals the interactions between HFE and Pyr^+ . Further adding $\text{Zn}(\text{TFSI})_2$ salt into the mixture of HFE and PyrTFSI causes almost no changes in chemical shift of ^1H NMR signals from HFE, again proving that HFE does not coordinate with Zn^{2+} . Electrospray ionization mass spectroscopy (ESI–MS) was also used to probe the solvation species in electrolyte solutions. Apart from $\text{Zn}(\text{TFSI})_2^+$ signal, a prominent peak ascribed to $\text{ZnTFSI}(\text{Pyr})$ ($m/z=487$) can be observed over a large mass-to-charge range in Zn–IL electrolyte (Figure 2d and e), which suggests the prevalence of TFSI-bridged ionic aggregates. Considering that transient disintegration of large ionic clusters usually occurs during the flight stage of the electrospraying process in ESI–MS tests,^[24] there is a high possibility that even larger aggregated ionic networks exist in Zn–IL. With the addition of HFE, the signal of $\text{ZnTFSI}(\text{Pyr})$ disappeared, inferring that the relatively large ionic aggregate networks are segmented into smaller

ones. Moreover, we further measured the Stokes radii of electrolytes based on the following Stokes-Einstein equation:^[22]

$$D = \frac{kT}{6\pi \cdot R \cdot \eta}$$

where k is the Boltzmann constant, T stands for temperature, η is the viscosity of electrolyte and R stands for the hydrodynamic radius, i.e., the so called Stokes radii. Stokes radii, which is sometimes used synonymously with effective hydrated radius in solution, represents the radius of a hard sphere that diffuses at the same rate as that solute. It is closely related to solute mobility, factoring in not only size but also solvent effects. Calculated results show that the Stokes radius of Zn–IL electrolyte is reduced from 1.3 nm to 0.97 nm after the addition of HFE (Table S1), which again proves that the large ionic network is broken apart into progressively smaller clusters. As a result, the prevalent electrostatic interactions between Zn^{2+} , TFSI^- and Pyr^+ confined in large ionic aggregates is weakened, which accounts for the reduced viscosity and enhanced Zn^{2+} mobility.

Rate capabilities of DIBs based on diluted IL electrolytes

The enhanced Zn^{2+} transport is expected to reduce the concentration polarization. The voltage profiles of Zn/Zn^{2+} at a current density of 0.1 mA cm^{-2} show that the overpotential of Zn deposition decreases from $\sim 0.27 \text{ V}$ in Zn–IL electrolyte to $\sim 0.12 \text{ V}$ in Zn–IL–HFE electrolyte (Figure 3a). The influence of HFE diluent on the Zn deposition can be also illustrated from

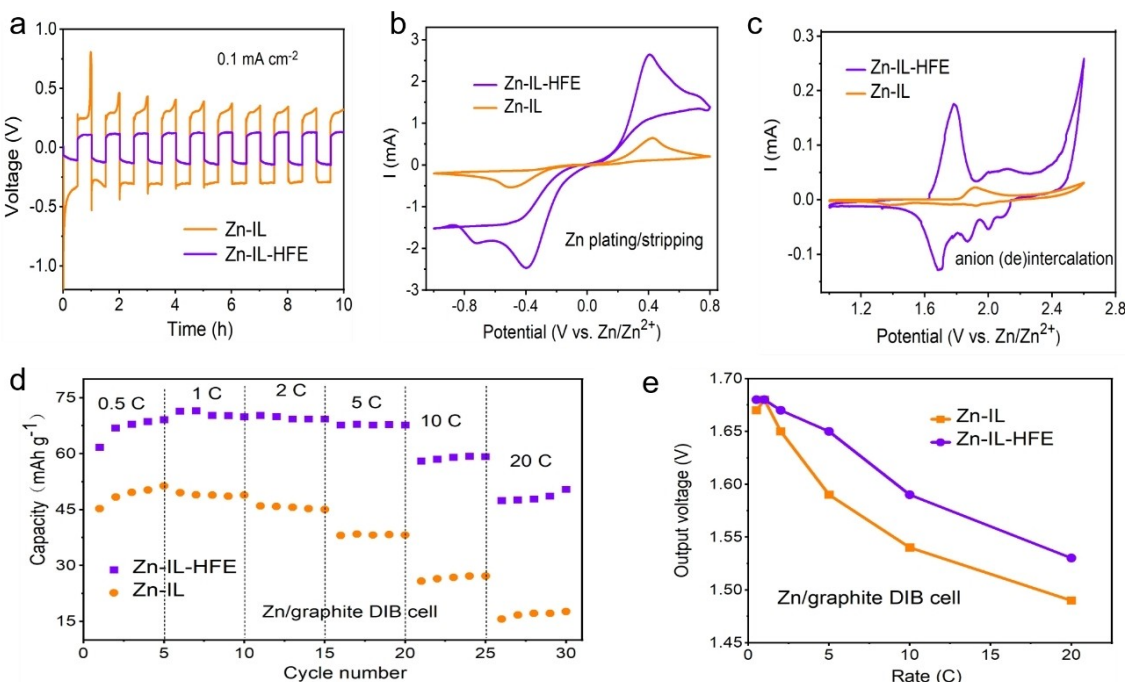


Figure 3. Electrochemical performance of electrolytes. a) Voltage profiles of Zn plating/stripping in Zn–IL and Zn–IL–HFE electrolytes tested in symmetric Zn/Zn coin cells at a current density of 0.1 mA cm^{-2} . b) CV curves of Zn plating/stripping on Ti foils measured at a scan rate of 0.5 mVs^{-1} in a three-electrode cell using Zn foils as the counter and reference electrodes. c) CV curves of anion (de)intercalation into graphite electrode in Zn–IL and Zn–IL–HFE electrolytes measured at a scan rate of 0.5 mVs^{-1} in a three-electrode cell using Zn foils as the counter and reference electrodes. d) Rate capabilities of Zn/graphite DIB cells tested at an upper voltage of 2.65 V . The capacity is calculated based on the mass of graphite. e) Average output voltages of Zn/graphite cells in Zn–IL and Zn–IL–HFE electrolytes at varied rates.

CV curves collected in a three-electrode cell using a Zn foil as the quasi-reference electrode. CV curves (third scan) of both Zn–IL and Zn–IL–HFE electrolytes are presented in Figure 3(b). It is shown that the Zn–IL–HFE electrolyte is able to support Zn plating and stripping with peak currents of 2.46 and 2.64 mA respectively at a sweep rate of 0.5 mVs^{-1} . On the other hand, the solution based on Zn–IL electrolyte achieved much lower peak currents for both Zn plating and stripping (0.53 and 0.64 mA , respectively) under identical conditions. In addition, the onset potential of TFSI^- intercalation into graphite cathode is also greatly reduced, i.e., from 1.82 V vs. Zn/Zn^{2+} in Zn–IL electrolyte to 1.63 V vs. Zn/Zn^{2+} in Zn–IL–HFE electrolyte (Figure 3c), which suggests that the HFE diluent brings additional benefit of enhancing the dynamics of TFSI^- . The cycled graphite cathodes in both Zn–IL and Zn–IL–HFE electrolytes display clean surface without amorphous cathode electrolyte interphase (CEI) layer (Figure S7), ruling out the possibility that the decreased onset potential of anion intercalation into graphite in Zn–IL–HFE electrolyte is related to the CEI.

Due to the lowered overpotential of both Zn plating/stripping and TFSI^- intercalation into graphite cathode after HFE dilution of Zn–IL electrolyte, the assembled Zn/graphite DIB cell using the Zn–IL–HFE electrolyte suffers from much less polarization as evidenced by the increased discharge capacity accompanied with elevated average output voltage (Figure S8). The rate performance of Zn/graphite DIB cells is displayed in Figure 3(d). As the charge/discharge rate increases from 0.5 C to 20 C , 71% discharge capacity retention is observed in

Zn–IL–HFE electrolyte. For comparison, the Zn/graphite cell based on the Zn–IL electrolyte retains only 34.5% of the initial capacity when the rate increases to 20 C . The large polarization caused by the insufficient ion mobility in Zn–IL also causes obvious decreases in output voltages at elevated rates. The average output voltage of Zn/graphite cell based on Zn–IL electrolyte gradually decreases from 1.68 V to 1.49 V when the rate increases from 1 C to 20 C (Figure 3e). In contrast, the Zn–IL–HFE electrolyte provides higher average discharge voltages (1.53 V at 20 C), which also exceeds those of typical Zn batteries (0.8 – 1.5 V) based on conventional manganese and vanadium oxide cathodes.^[25] Due to increased discharge capacity and output voltage, the Zn/graphite DIB based on the Zn–IL–HFE electrolyte delivers much higher energy density and power density than that using Zn–IL electrolyte, especially at elevated rates (Table 1).

Electrochemical reversibility at high DOD_{Zn}

Apart from rate capability, superior cycling performance, especially at high utilization rate of Zn anode, is also crucial for the commercial competitiveness of Zn/graphite DIBs. The Coulombic efficiency (CE) of Zn plating/stripping, a critical parameter responsible for the redox reversibility, was first investigated with a small galvanostatic capacity of 0.09 mAh cm^{-2} . After a gradual rise in the initial 100 cycles, the average CE of Zn plating/stripping in Zn–IL–HFE electrolyte

Table 1. Electrochemical performance of Zn/graphite DIBs using Zn–IL and Zn–IL–HFE electrolytes in a voltage range of 2.65–1.20 V. All of these values are calculated based on the mass of graphite.

Electrolyte	Rate [C]	Discharge capacity [mAh g^{-1}]	Energy density [Wh kg^{-1}]	Power density [kW kg^{-1}]
Zn–IL	5	38.4	61.1	0.31
	10	26.4	40.7	0.41
	20	16.7	24.9	0.50
Zn–IL–HFE	5	67.9	112	0.56
	10	58.5	93.0	0.93
	20	47.6	72.8	1.46

stabilizes at ~99.9% in the subsequent 1900 cycles (Figure 4a), demonstrating the high reversibility of Zn plating/stripping at a low areal capacity. In the case of Zn–IL electrolyte, although the average CE is also retained at a high value of 99.7%, the appearance of “spikes” in current profile suggests the formation of “dead” Zn. This phenomenon is usually associated with noncompact and loose Zn deposition which permits the diffusion of electrolytes to the roots of Zn deposits and eventually causes Zn dissolution from the bottom during the stripping process.^[26] The CE evaluation of metal plating/stripping has a great dependence on the deposition substrate, concerning their intrinsic physicochemical properties as well as the surface roughness.^[27] Hence, besides Ti foil, Cu foil and stainless steel foil were also used as the substrates for Zn deposition during CE tests. Although the average CEs of Zn plating/stripping on Cu foil and stainless steel foil are lower compared with that in Ti foil substrate, the trend of improved

reversibility of Zn plating/stripping in Zn–IL–HFE electrolyte still applies (Figures S9).

For practical rechargeable Zn batteries, the depth of Zn discharge (DOD_{Zn}) is an even more important metric since it determines how much of the promised high energy density can be realized at the device level. It should be pointed out that the above cycling tests of Zn electrodes were performed at an extremely low depth of discharge of Zn electrode (~0.002% DOD_{Zn}). Although evaluating the cycling performance of Zn metal cells at low DOD_{Zn} is widely used in academia, the severely inadequate utilization efficiency of Zn metal anodes greatly reduces the energy density of the battery.^[17] As a result, the test data of Zn reversibility at low DOD_{Zn} often deviates significantly from what is needed for practical applications, i.e., high DOD_{Zn} .

Hence, further interrogation of Zn reversibility in the Zn–IL–HFE electrolyte was carried out by deep-discharge tests (60% and 80% DOD_{Zn}) in asymmetrical Zn/Cu cells. Figure 4(b) displays the cycling performance of Zn electrode at 60% DOD_{Zn} at a current density of 0.1 mA cm^{-2} . With Zn–IL electrolyte, the cell at 60% DOD_{Zn} failed after just 14 cycles (786 h). By contrast, the Zn–IL–HFE electrolyte sustains the cycling of the cell for 4021 h. When the utilization rate of Zn electrode is increased to 80% DOD_{Zn} during the test, the cell in Zn–IL electrolyte failed at the 9th cycle (600 h), while in the Zn–IL–HFE electrolyte, stable Zn plating/stripping can be maintained for ~4015 h under the identical testing conditions, demonstrating the capability of the Zn–IL–HFE electrolyte to support highly reversible Zn plating/stripping with a high Zn utilization rate per cycle. Normally, the stable cycle number of repeated Zn

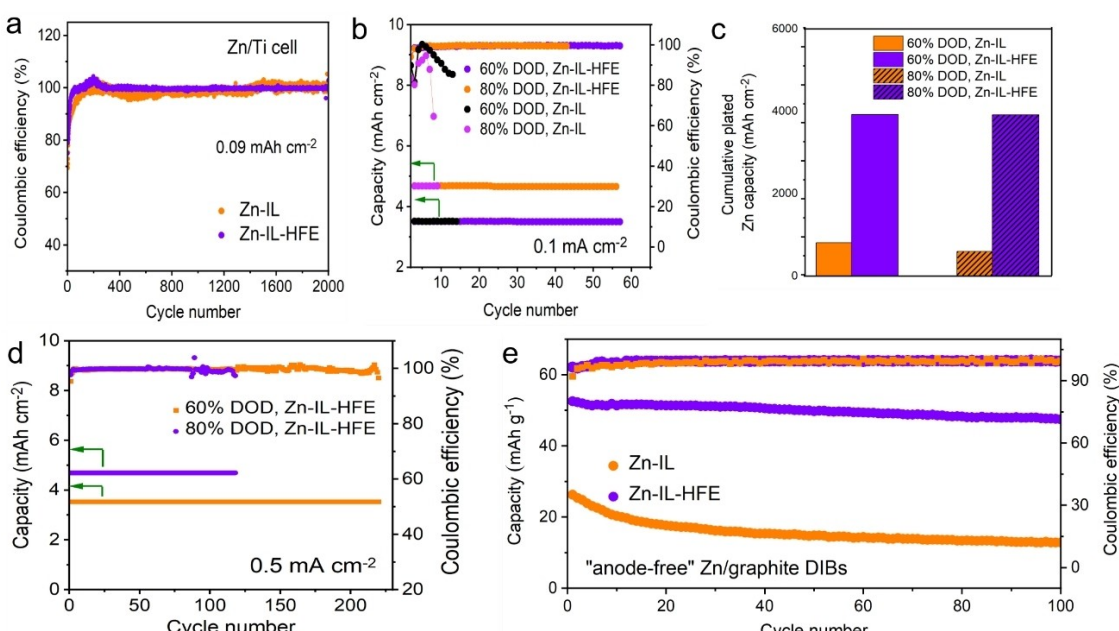


Figure 4. Reversibility of Zn plating/stripping at various depth of discharge of Zn anodes (DOD_{Zn}). a) CE of Zn plating/stripping on a Ti foil at merely 0.002% DOD_{Zn} with a low areal capacity of 0.09 mAh cm^{-2} . b) Cycling performance of Zn plating/stripping in Zn/Cu cells at 60% and 80% DOD_{Zn} at a current density of 0.1 mA cm^{-2} . c) Relationship between DOD_{Zn} , electrolyte composition and cumulative galvanic capacity. d) Cycling performance of Zn plating/stripping at 60% and 80% DOD_{Zn} at a current density of 0.5 mA cm^{-2} in Zn–IL–HFE electrolyte. e) Cycling performance of “anode-free” Zn/graphite DIBs at rate of 5 C in a voltage range of 2.65–1.2 V. The “anode-free” Zn/graphite DIB use a Cu foil as anode substrate.

plating/stripping would reduce at higher DOD_{Zn} associated with elevated areal capacity during each cycle. Indeed, the compiled results of Zn plating/stripping in Zn–IL electrolyte show that the stable cycle number sharply decreases from 14 to 9 as the areal capacity increases from 3.41 mAh cm⁻² to 4.66 mAh cm⁻² (Figure S10). On the other hand, the cycle number decreases slightly from 57 to 43 for the Zn–IL–HFE electrolyte at elevated areal capacity, which reveals more compact and uniform Zn deposition. To achieve a competitive commercial rechargeable Zn metal battery, a relatively high cumulative capacity of plated Zn is desired. The cumulative capacity of plated Zn sharply increases at elevated areal capacity during each cycle, and eventually reaches ~3919 mAh cm⁻² at areal capacity of 4.64 mAh cm⁻² (80% DOD_{Zn}) in the presence of Zn–IL–HFE electrolyte (Figure 4c). This value is six times higher than that based on Zn–IL electrolyte (600 mAh cm⁻²), which shows much more promise in practical Zn batteries. More stringent deep-discharge tests of Zn electrodes were evaluated at a higher current density of 0.5 mA cm⁻². Zn deposition in Zn–IL electrolyte suffers from open circuit in the first cycle due to the constantly increased overpotential (Figure S11). In comparison, the cell based on Zn–IL electrolyte could sustain the stable Zn plating/stripping for 219 and 120 cycles at 60% DOD_{Zn} and 80% DOD_{Zn} respectively (Figure 4d), further proving the much higher reversibility of Zn plating/stripping in Zn–IL–HFE electrolyte, especially at elevated current densities.

Most previous work of Zn/graphite DIBs has adopted cell configuration based on Zn metal anode, which leads to substantial underutilization of Zn electrode since the electrolyte could serve as a reservoir of active Zn²⁺ for Zn deposition on a substrate during charge.^[4b,14,28] Although this configuration using a large excess of Zn anode could maintain decent cycling stability of Zn/graphite DIBs in the case of high-stability electrolytes, it is impractical for commercial applications. Recently, the concept of “anode-free” Zn/graphite DIBs has been developed by Feng et al. using a silver-coated Cu substrate as the current collector,^[29] which leads to much improved energy density compared with the conventional Zn/graphite DIBs based on Zn metal anode. However, the use of silver as coating materials would inevitably increase the cost of Zn/graphite DIBs. Although highly concentrated electrolytes such as 3 M Zn(TFSI)₂/EMC is reported to display high anodic stability, the assembled Zn/graphite DIB without Zn metal delivers an average CE of only ~77% (Figure S12), which reveals the challenges of anode-free Zn/graphite DIBs. Here, anode-free Zn/graphite DIBs were assembled using Cu as anode current collector and graphite as the cathode to demonstrate the effect of HFE diluent on the deep discharge capability of the Zn anode in full cells. The anode-free Zn/graphite DIB using Zn–IL electrolyte has an average CE of only 97% in the first 30 cycles. After 100 cycles, the delivered specific capacity reduces to 15 mAh g⁻¹ with a capacity retention of only 32%. In comparison, the assembled cell based on the Zn–IL–HFE electrolyte maintains 90% initial capacity with an average CE of ~99.9% after 100 cycles (Figure 4e),

which proves the feasibility of Zn–IL–HFE electrolyte for anode-free Zn/graphite DIBs.

Morphological characterizations of Zn deposits

Zn reversibility at high DOD_{Zn} is closely correlated with the morphology of Zn deposition since the noncompact deposition tends to cause the formation of dead Zn during the stripping process. Therefore, the surface morphology of Zn deposition in different electrolytes are characterized using multi-scale observations. SEM images in Figure 5(a) show that Zn deposits in the presence of Zn–IL electrolyte are full of unevenly distributed agglomerated particles with large sizes. SEM images at higher magnification reveal that these agglomerated Zn particles are randomly oriented with the presence of large amounts of pores and voids between them. Visually, the deposited Zn displays an appearance of inhomogeneous black powder with protrusions, which suggests their non-uniformity. In sharp contrast, the deposited Zn layer from Zn–IL–HFE electrolyte is smooth and compact, which consists of platelets stacked compactly without pores or voids. Accordingly, the Zn deposits is visually uniform with gray color. In addition, it is noted that the compactly stacked platelets preferentially exposing the basal plane of (002) aligns vertical with respect to the electrode surface, which can be more clearly observed in SEM images at higher magnifications and confirmed by XRD analysis (Figures S13 and S14). The phenomenon of vertical alignment of Zn deposits is similar to recent findings by Archer et al., who propose that the plate-like Zn electrodeposits may undergo a reorientation transition to maximize access to the supply of ions just outside the depletion zone.^[15] When Zn foil substrate is replaced with Ti foil or Cu foil, the uniform and compact Zn deposition in Zn–IL–HFE electrolyte can be still observed (Figure S15). However, it is noted that the deposited Zn is not vertical with respect to the electrode surface from magnified SEM images (Figure S16), which is likely related to the lattice matching of deposited Zn and substrate materials in the initial nucleation stage.

The side-views further provide stacking morphologies of deposited Zn. Cross-sectional SEM imaging in Figure 5(b) shows that the thickness of the deposited Zn in Zn–IL electrolyte is 15 µm at a capacity of 2 mAh accompanied with large amounts of voids due to noncompact stacking. By contrast, a much thinner deposited Zn layer (11 µm) is observed in Zn–IL–HFE electrolyte, which proves the more uniform and denser Zn deposition. The uniformity of Zn deposits can be also evaluated by the root mean square (RMS) roughness of Zn deposits using confocal laser scanning microscopy (CLSM). Figure 5(c) shows that RMS roughness of deposited Zn in Zn–IL electrolyte is 32.9 µm, and this value was reduced to 18.7 µm when the Zn deposition occurs in Zn–IL–HFE electrolyte. To better present the surface morphology of Zn deposits at much higher resolution, atomic force microscopy (AFM) was also employed to observe the morphologies of Zn surface. Figure 5(d) shows that the deposited Zn obtained in Zn–IL electrolyte contains many pores and voids between Zn particles accompanied with

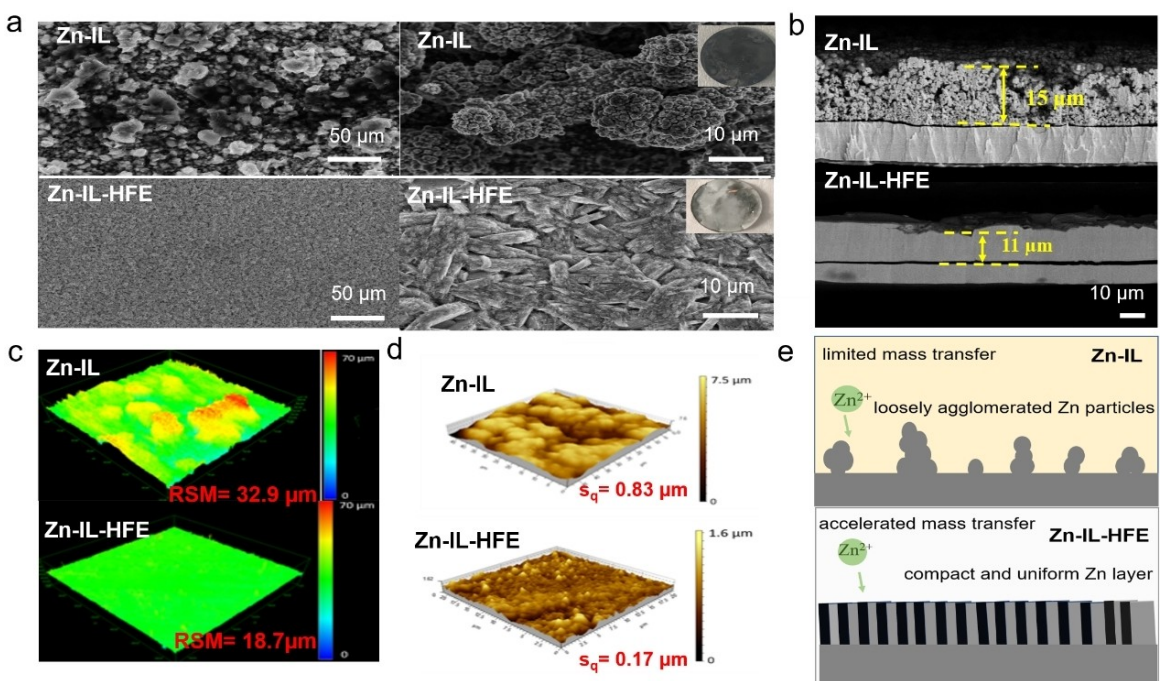


Figure 5. Morphology characterizations of Zn electrodeposits in Zn-IL and Zn-IL-HFE electrolytes. a) Typical SEM images of Zn deposits on Zn foils using Zn-IL and Zn-IL-HFE electrolytes. The Zn deposits were obtained by plating at a current density of 0.2 mA cm^{-2} with areal capacity of 2 mAh cm^{-2} . The insets display the optical photos of Zn deposits on Zn foils. b) Cross-sectional SEM images and EDS-mapping of Zn deposits at a capacity of 2 mAh obtained in Zn-IL and Zn-IL-HFE electrolytes. c) Atomic force microscopy (AFM) to obtain topographic surface images and roughness (S_q) of Zn deposits in Zn-IL and Zn-IL-HFE electrolytes. d) Confocal laser scanning microscopy (CLSM) images and corresponding root mean square (RMS) roughness of Zn deposits obtained in Zn-IL and Zn-IL-HFE electrolytes. e) Schematic of the Zn deposition process in Zn-IL and Zn-IL-HFE electrolytes.

a high rough surface ($S_q = 0.83 \mu\text{m}$). In comparison, Zn deposition occurring in Zn-IL-HFE electrolyte presents a more uniform surface with smaller roughness ($S_q = 0.17 \mu\text{m}$). In short, the addition of HFE into Zn-IL electrolyte facilitates the mass transfer of Zn^{2+} and leads to more compact and uniform Zn deposition as illustrated in Figure 5(e).

Mechanistic insights into compact Zn deposition in Zn-IL-HFE electrolyte

A further question concerns why the addition of HFE into Zn-IL electrolyte results in more compact and uniform Zn deposition. It is well established that the morphology of Zn electrodeposition is mainly governed by factors including SEI, interface reaction kinetics and rate of mass transport, all of which are closely related to the electrolyte compositions.^[26,30] SEI has received enormous attention in recent years because of its hypothetical role in promoting uniform metal deposition, although the detailed mechanism in regulating the morphology of metal electrodeposits remains controversial.^[31] In our case, Raman and IR spectra of cycled Zn anodes in both the in Zn-IL and Zn-IL-HFE electrolytes do not show signals of characteristic SEI components on Zn anode such as ZnF_2 and organic functional groups (S=O, C=N) (Figures S17 and S18). These results signify the non-existence of SEI layer of Zn anode and thus rule out the possible role of SEI in contributing to the compact Zn deposition in the Zn-IL-HFE electrolyte.

It is generally agreed that a moderately small exchange current (slow reaction kinetics) and large diffusion-limited current density (high electrolyte ion diffusivity) could alleviate the concentration polarization and promote relatively compact Zn electrodeposition.^[26] Considering that the addition of HFE leads to reduced viscosity and increased Zn^{2+} transport ability, it is speculated that the compact Zn deposition in Zn-IL-HFE electrolyte originates from alleviated concentration polarization. To confirm it, CV curves of Zn plating/stripping in Zn-IL electrolyte at a series of scan rates were collected. According to the Berzin-Delahay's equation,^[32] we plot j_p vs. $v^{1/2}$ (Figures 6a and S19), which follows the perfect linear relation, revealing the diffusion-controlled Zn electrodeposition in Zn-IL electrolyte. The Zn deposition using an electrolytic cell under the constant stirring of electrolyte to assist the mass transport further verified our hypothesis. As shown in Figure 6(b), the overpotential of Zn plating in Zn-IL electrolyte without stirring increases constantly and eventually exceeds the voltage limits of battery tester (6 V) in merely 40 min at a current density of 0.5 mA cm^{-2} , which demonstrates the depletion of active Zn^{2+} species on electrode surface. At a stirring rate of 50 rpm, the available Zn deposition time before battery failure is extended to 83 min. At a higher rotation rate of 500 rpm with more turbulent electrolyte convection, the limiting regions of Zn deposition is noticeably absent, signifying mass transport-governed electrodeposition of Zn. Accordingly, Zn deposits obtained in the Zn-IL electrolyte under higher stirring rates display more uniform and compact surface morphology due to

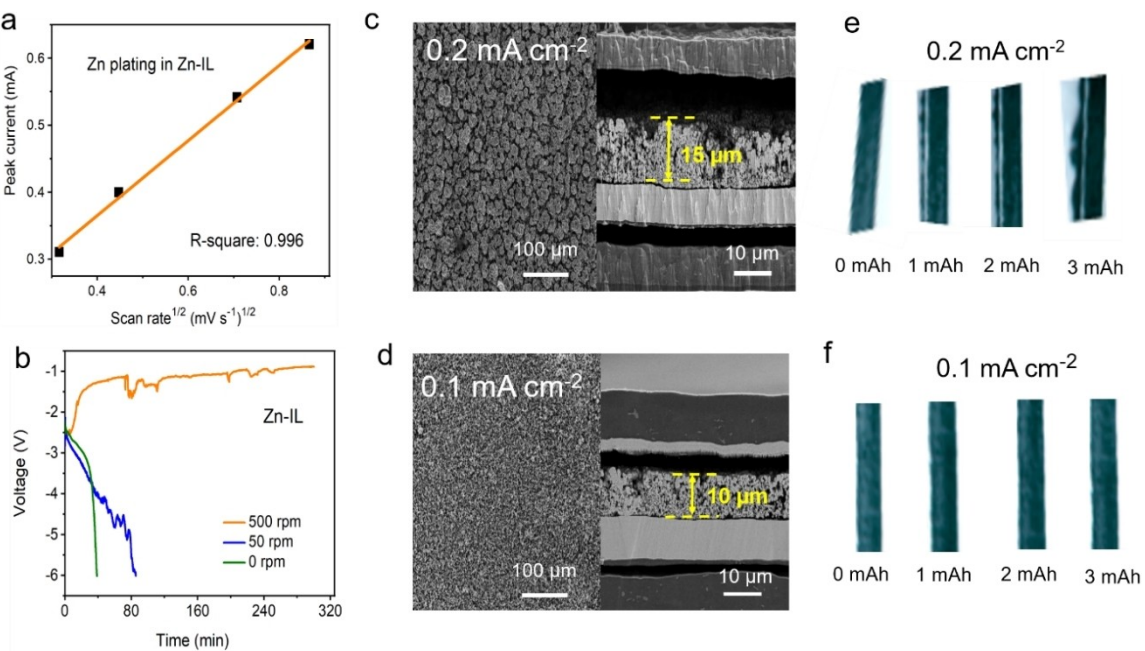


Figure 6. The influence of Zn^{2+} transport ability in ionic liquid electrolyte on Zn electrodeposition. a) Plot of peak current of Zn deposition in Zn–IL electrolyte versus scan rate $^{1/2}$ according to Berzins–Delahay's equation obtained from CV tests. CV tests of Zn stripping/deposition in Zn–IL electrolyte were performed using a three-electrode cell with Zn metal foil as the counter and reference electrodes and Cu foil as working electrode. b) Voltage profiles of Zn deposition on a Cu substrate at varied stirring rates of Zn–IL electrolytes. The tests were performed using a three-electrode cell with Cu foil as working electrode and Zn foil as the counter and reference electrode at a current density of 1 mA cm^{-2} . Typical SEM images and corresponding cross-sectional views of Zn deposits using Zn–IL electrolytes at a current density of c) 0.2 mA cm^{-2} and d) 0.1 mA cm^{-2} . In situ optical microscopic images of the Zn electrodeposition process in Zn–IL electrolyte at a current density of e) 0.2 mA cm^{-2} and f) 0.1 mA cm^{-2} .

the alleviated concentration gradient (Figure S20). The diffusion-controlled Zn deposition in Zn–IL electrolyte due to insufficient Zn transport ability can be also confirmed by recording the evolution of overpotential of Zn deposition at varied current densities. Figure S21 shows that the Zn plating/stripping proceeds normally in the first two cycles at a small current density of 0.1 mA cm^{-2} , albeit a sharp decrease of overpotential is observed in the first cycle due to the nucleation process. When the current density is increased to 0.5 mA cm^{-2} in the third cycle, the overpotential of Zn plating increases sharply and leads to battery failure, which demonstrates the depletion of active Zn^{2+} species on electrode surface. After left standing for 6 h to replenish the Zn^{2+} on electrode surface, Zn deposition could proceed again, demonstrating that the deposition in the IL electrolyte is diffusion-controlled.

Apart from electrochemical techniques, the diffusion-controlled Zn deposition in Zn–IL electrolyte can be also illustrated from morphological characterizations. By adjusting the current density, the effect of Zn^{2+} mass transport on the deposition morphology was evaluated in IL electrolyte. At a current density of 0.2 mA cm^{-2} , the Zn deposits in Zn–IL electrolyte are composed of porous agglomerated particles loosely stacked with a thickness of $\sim 15 \mu\text{m}$ (Figure 6c). When the current density is reduced to 0.1 mA cm^{-2} , more uniform and denser Zn deposition with a thickness of only $\sim 10 \mu\text{m}$ can be observed (Figure 6d). If the current density is elevated to 0.5 mA cm^{-2} , the Zn deposits become unevenly distributed with large

amounts of voids (Figure S22). Two additional surface-sensitive techniques (AFM and LSCM) were also used to probe the deposited Zn at varied current densities. Not surprisingly, as the current density decreases from 0.2 mA cm^{-2} to 0.1 mA cm^{-2} , the value of surface roughness (obtained from AFM) and root mean square (RMS) roughness (obtained from LSCM) of Zn deposits becomes smaller (Figures S23 and S24), confirming more uniform and compact Zn deposition with less protrusions due to alleviated concentration gradient. It should be noted that even at a small current density of 0.1 mA cm^{-2} , the surface roughness of Zn deposits is still significantly larger than that of pristine Zn foil (Figure S25). Additional evidence for the more uniform Zn deposition at lower current densities can be provided by in situ optical visualization observations of Zn deposition in a home-made cell (Figure S26). Uneven Zn electrodeposits were observed under a current density of 0.2 mA cm^{-2} (Figure 6e). By contrast, Zn surface after deposition remain visibly flat in a low current density 0.1 mA cm^{-2} (Figure 6f), which emphasizes a strong correlation between the effective Zn^{2+} diffusion rate and uniform Zn deposition.

In short, due to the diffusion-controlled Zn deposition in highly viscous Zn–IL electrolyte, Zn deposition tends to occur on the tips of electrode surface to maximize access to the supply of ions, especially at elevated current densities, which accounts for the rough and nonplanar morphologies of Zn^{2+} deposits. Upon the addition of HFE diluent, diffusion coefficient is increased by 30 times, which alleviates the concentration gradient. Consequently, more compact and uniform Zn deposi-

tion occurs. Apart from diffusion coefficient, transference number is another important parameter that control the transport dynamics. The transference numbers of Zn^{2+} were obtained by using the conventional potentiostatic polarization method developed by Vincent and Bruce,^[33] which is slightly reduced from 0.63 in Zn–IL electrolyte to 0.58 upon the addition of HFE diluent (Table 2 and Figure S27). This suggests that the introduced HFE does not alter the solvation sheath of Zn^{2+} remarkably, in agreement with previous solvation structure results that HFE does not coordinate with Zn^{2+} . The relative rate of Zn^{2+} transport ability to the rate of Zn^{2+} electrochemical reduction at the interface can be quantitatively described by Sand's time (T_{Sand}), which refers to the time of Zn^{2+} depletion near plain electrode surface at an over-limiting current density. Sand's time can be calculated using the following formula:^[34]

$$T_{\text{Sand}} = \pi D \frac{(Z_c C_0 F)^2}{4(J(1 - t_+))^2}$$

Z_c , F , and J correspond to the charge of Zn^{2+} , Faraday's constant, and current density applied, respectively. While c_0 , t_+ and D in Sand formula refer to the concentration, transference number, and diffusion coefficient of Zn^{2+} , respectively. The estimated Sand's times for the Zn–IL and Zn–IL–HFE electrolytes are determined to be 83 and 1963 s, respectively (Table 2). The higher Sand's time in Zn–IL–HFE corresponds to improved Zn^{2+} transport ability, which promotes more uniform and compact Zn deposition.

Conclusions

To overcome the poor rate capability and inferior cycling performance of Zn/graphite DIBs at a high utilization rate Zn anode in typical Zn-based ionic liquid electrolyte, HFE featuring low viscosity and high anodic stability was added as diluent to improve the Zn^{2+} transport ability while not compromise its oxidation stability. The introduced HFE co-solvent interactions with Pyr^+ and thus weakens the extensive ionic interactions among different species confined in ionic aggregate clusters, which results in the breaking down the larger ionic aggregates in IL. Consequently, the viscosity is greatly reduced, which leads to the increase of diffusion coefficient of Zn^{2+} up to ~30 times. One direct result of this solvation change is concerned with the drastic improvement in Zn^{2+} transport ability, which greatly lowers the high overpotential of Zn plating/stripping usually encountered in IL. Consequently, the rate capability of the Zn/graphite DIB cell is improved remarkably. The accelerated mass

Table 2. Comparison of Zn^{2+} transport ability in Zn–IL and Zn–IL–HFE electrolytes.

Electrolyte	Diffusion coefficient of Zn^{2+} [$10^{-9} \text{ cm}^2 \text{s}^{-1}$]	Transference number of Zn^{2+}	Sand's time [s]
Zn–IL	2.4	0.63	83
Zn–IL–HFE	74	0.58	1963

transfer of active Zn species upon the addition of HFE also alleviates the concentration polarization, which promotes compact and uniform Zn deposition as evidenced by SEM, cross-section, AFM, and LSCM characterizations. The high-depth discharge of Zn anode with 130 cycles accompanied with a cumulative areal capacity, which represents 20 times increase compared with the typical Zn–IL electrolyte. The high reversibility of Zn plating/stripping at a high areal capacity also enables the operation of “anode-free” Zn/graphite DIB cell, which maintains 90% capacity after 100 cycles. To the best of our knowledge, this is the first successful attempt to improve the mass transfer of active species in electrolytes for Zn/graphite DIBs while not sacrificing their oxidation stability.

Acknowledgements

This work was financially supported by National Key R&D Program of China (2022YFB2402600), National Natural Science Foundation of China (22209194, 52072195), and Shandong Natural Science Foundation (ZR2020ZD07 and ZR2021QB106).

Conflict of Interest

The authors declare no conflict of interest.

Data Availability Statement

The data that support the findings of this study are available from the corresponding author upon reasonable request.

Keywords: hydrofluoroether · ionic liquid · Zn deposition · Zn/graphite battery · Zn^{2+} transport ability

- [1] B. Dunn, H. Kamath, J. M. Tarascon, *Science* **2011**, *334*, 928–935.
- [2] a) K. V. Kravchyk, M. V. Kovalenko, *Adv. Energy Mater.* **2019**, *9*, 1901749; b) M. Wang, Y. B. Tang, *Adv. Energy Mater.* **2018**, *8*, 1703320; c) Y. Zhao, K. M. Xue, T. Tan, D. Y. W. Yu, *ChemSusChem* **2023**, *16*, e202201221; d) M. Q. Liu, W. Zhang, W. T. Zheng, *ChemSusChem* **2023**, *16*, e202201375.
- [3] G. Wang, M. H. Yu, J. G. Wang, D. B. Li, D. M. Tan, M. Loffler, X. D. Zhuang, K. Mullen, X. L. Feng, *Adv. Mater.* **2018**, *30*, 1800533.
- [4] a) J. A. Seel, J. R. Dahn, *J. Electrochem. Soc.* **2000**, *147*, 892–898; b) Z. Chen, T. M. Liu, Z. M. Zhao, Z. H. Zhang, X. Q. Han, P. X. Han, J. D. Li, J. Z. Wang, J. J. Li, S. Q. Huang, X. H. Zhou, J. W. Zhao, G. L. Cui, *J. Power Sources* **2020**, *457*, 227994; c) X. Lei, Y. P. Zheng, F. Zhang, Y. Wang, Y. B. Tang, *Energy Storage Mater.* **2020**, *30*, 34–41; d) M. Wang, C. L. Jiang, S. Q. Zhang, X. H. Song, Y. B. Tang, H. M. Cheng, *Nat. Chem.* **2018**, *10*, 667–672; e) M. C. Lin, M. Gong, B. G. Lu, Y. P. Wu, D. Y. Wang, M. Y. Guan, M. Angell, C. X. Chen, J. Yang, B. J. Hwang, H. J. Dai, *Nature* **2015**, *520*, 325–328.
- [5] a) L. E. Blanc, D. Kundu, L. F. Nazar, *Joule* **2020**, *4*, 771–799; b) D. L. Chao, W. H. Zhou, F. X. Xie, C. Ye, H. Li, M. Jaroniec, S. Z. Qiao, *Sci. Adv.* **2020**, *6*, eaba4098; c) D. Xie, Z. W. Wang, Z. Y. Gu, W. Y. Diao, F. Y. Tao, C. Liu, H. Z. Sun, X. L. Wu, J. W. Wang, J. P. Zhang, *Adv. Funct. Mater.* **2022**, *32*, 2204066; d) D. Xie, Y. Sang, D. H. Wang, W. Y. Diao, F. Y. Tao, C. Liu, J. W. Wang, H. Z. Sun, J. P. Zhang, X. L. Wu, *Angew. Chem. Int. Ed.* **2023**, *62*, e202216934.

- [6] a) H. Z. Jiang, Z. Chen, Y. Y. Yang, C. Fan, J. W. Zhao, G. L. Cui, *ChemSusChem* **2023**, *16*, e202201561; b) T. Placke, A. Heckmann, R. Schmuck, P. Meister, K. Beltrop, M. Winter, *Joule* **2018**, *2*, 2528–2550.
- [7] X. Y. Jiang, L. B. Luo, F. P. Zhong, X. M. Feng, W. H. Chen, X. P. Ai, H. X. Yang, Y. L. Cao, *ChemElectroChem* **2019**, *6*, 2615–2629.
- [8] a) M. Armand, F. Endres, D. R. MacFarlane, H. Ohno, B. Scrosati, *Nat. Mater.* **2009**, *8*, 621–629; b) D. R. Macfarlane, M. Forsyth, P. C. Howlett, J. M. Pringle, J. Sun, G. Annat, W. Neil, E. I. Izgorodina, *Acc. Chem. Res.* **2007**, *40*, 1165–1173.
- [9] F. Endres, *ChemPhysChem* **2002**, *3*, 144–154.
- [10] a) R. T. Carlin, H. C. Delong, J. Fuller, P. C. Trulove, *J. Electrochem. Soc.* **1994**, *141*, L73–L76; b) T. Placke, O. Fromm, S. F. Lux, P. Bieker, S. Rothermel, H. W. Meyer, S. Passerini, M. Winter, *J. Electrochem. Soc.* **2012**, *159*, A1755–A1765; c) S. Rothermel, P. Meister, G. Schmuelling, O. Fromm, H. W. Meyer, S. Nowak, M. Winter, T. Placke, *Energy Environ. Sci.* **2014**, *7*, 3412–3423.
- [11] a) T. J. Simons, D. R. MacFarlane, M. Forsyth, P. C. Howlett, *ChemElectroChem* **2014**, *1*, 1688–1697; b) M. Tulodziecki, J. M. Tarascon, P. L. Taberna, C. Guery, *J. Electrochem. Soc.* **2012**, *159*, D691–D698; c) M. Xu, D. G. Ivey, Z. Xie, W. Qu, *Electrochim. Acta* **2013**, *89*, 756–762.
- [12] K. Angenendt, P. Johansson, *J. Phys. Chem. B* **2011**, *115*, 7808–7813.
- [13] a) N. N. Rajput, T. J. Seguin, B. M. Wood, X. H. Qu, K. A. Persson, *Top. Curr. Chem.* **2018**, *376*, 19; b) S. H. Lapidus, N. N. Rajput, X. H. Qu, K. W. Chapman, K. A. Persson, P. J. Chupas, *Phys. Chem. Chem. Phys.* **2014**, *16*, 21941–21945.
- [14] Z. Chen, Y. Tang, X. F. Du, B. B. Chen, G. L. Lu, X. Q. Han, Y. J. Zhang, W. H. Yang, P. X. Han, J. W. Zhao, G. L. Cui, *Angew. Chem. Int. Ed.* **2020**, *59*, 21769–21777; *Angew. Chem.* **2020**, *132*, 21953–21961.
- [15] J. C. Zheng, J. F. Yin, D. H. Zhang, G. J. Li, D. C. Bock, T. Tang, Q. Zhao, X. T. Liu, A. Warren, Y. Deng, S. Jin, A. Marschilok, E. S. Takeuchi, K. J. Takeuchi, C. D. Rahn, L. A. Archer, *Sci. Adv.* **2020**, *6*, eabb1122.
- [16] J. X. Zheng, T. Tang, Q. Zhao, X. T. Liu, Y. Deng, L. A. Archer, *ACS Energy Lett.* **2019**, *4*, 1349–1355.
- [17] L. Ma, M. A. Schroeder, O. Borodin, T. P. Pollard, M. S. Ding, C. S. Wang, K. Xu, *Nat. Energy* **2020**, *5*, 743–749.
- [18] Y. H. Chen, H. W. Yeh, N. C. Lo, C. W. Chiu, I. W. Sun, P. Y. Chen, *Electrochim. Acta* **2017**, *227*, 185–193.
- [19] a) Z. C. Wang, F. R. Zhang, Y. Y. Sun, L. Zheng, Y. B. Shen, D. S. Fu, W. F. Li, A. R. Pan, L. Wang, J. J. Xu, J. C. Hu, X. D. Wu, *Adv. Energy Mater.* **2021**, *11*, 2003752; b) K. Dokko, N. Tachikawa, K. Yamauchi, M. Tsuchiya, A. Yamazaki, E. Takashima, J. W. Park, K. Ueno, S. Seki, N. Serizawa, M. Watanabe, *J. Electrochem. Soc.* **2013**, *160*, A1304–A1310.
- [20] a) H. Lu, Y. Yuan, K. Zhang, F. R. Qin, Y. Q. Lai, Y. X. Liu, *J. Electrochem. Soc.* **2015**, *162*, A1460–A1465; b) C. C. Su, M. N. He, R. Amine, K. Amine, *Angew. Chem. Int. Ed.* **2019**, *58*, 10591–10595; *Angew. Chem.* **2019**, *131*, 10701–10705.
- [21] Y. Zhao, T. H. Zhou, T. Ashirov, M. El Kazzi, C. Cancellieri, L. P. H. Jeurgens, J. W. Choi, A. Coskun, *Nat. Commun.* **2022**, *13*, 2575.
- [22] K. Xu, *Chem. Rev.* **2004**, *104*, 4303–4417.
- [23] A. Bard, L. Faulkner, *Electrochemical Methods: Fundamentals and Applications*, 2nd ed., Wiley, New York, 2001.
- [24] B. P. Pozniak, R. B. Cole, *J. Am. Soc. Mass Spectrom.* **2015**, *26*, 369–385.
- [25] A. Konarov, N. Voronina, J. H. Jo, Z. Bakenov, Y. K. Sun, S. T. Myung, *ACS Energy Lett.* **2018**, *3*, 2620–2640.
- [26] J. X. Zheng, L. A. Archer, *Sci. Adv.* **2021**, *7*, eabe0219.
- [27] Z. J. Zhang, X. Yang, P. Li, Y. Wang, X. Zhao, J. Safaei, H. Tian, D. Zhou, B. H. Li, F. Y. Kang, G. X. Wang, *Adv. Mater.* **2022**, *34*, 2206970.
- [28] G. Wang, B. Kohn, U. Scheler, F. X. Wang, S. Oswald, M. Loffler, D. M. Tan, P. P. Zhang, J. Zhang, X. L. Feng, *Adv. Mater.* **2020**, *32*, 1905681.
- [29] G. Wang, M. S. Zhu, G. B. Chen, Z. Qu, B. Kohn, R. Scheler, X. Y. Chu, Y. B. Fu, O. G. Schmidt, X. L. Feng, *Adv. Mater.* **2022**, *34*, 2206970.
- [30] W. J. Lu, C. X. Xie, H. M. Zhang, X. F. Li, *ChemSusChem* **2018**, *11*, 3996–4006.
- [31] H. Y. Qiu, X. F. Du, J. W. Zhao, Y. T. Wang, J. W. Ju, Z. Chen, Z. L. Hu, D. P. Yan, X. H. Zhou, G. L. Cui, *Nat. Commun.* **2019**, *10*, 5347.
- [32] T. Berzins, P. Delahay, *J. Am. Chem. Soc.* **1953**, *75*, 555–559.
- [33] J. Evans, C. A. Vincent, P. G. Bruce, *Polymer* **1987**, *28*, 2324–2328.
- [34] H. J. S. Sand, *Philos. Mag.* **1901**, *1*, 45–79.

Manuscript received: February 17, 2023

Revised manuscript received: March 24, 2023

Accepted manuscript online: March 31, 2023

Version of record online: April 27, 2023